



OPEN

A static precise single-point positioning method based on carrier phase zero-baseline self-differencing

Kaihui Lv¹, Chenglin Cai^{2✉}, Yihao Cai^{4,5}, Wenhui Guan^{1✉}, Zexian Li³, Mingjie Wu² & Lingfeng Cheng²

Satellite navigation positioning has become an indispensable component of everyday life, where precise pinpointing and rapid convergence are crucial in delivering timely and accurate location information. However, due to the damping of integer ambiguities and system residual errors, the rapid convergence of Precise Point Positioning (PPP) implementation is a significant challenge. To address this, this paper proposes a novel Carrier Phase Zero-Baseline Self-Differencing Precise Point Positioning (CZS-PPP) technique and its ionosphere-free fusion model. By employing the proposed CZS-PPP approach in separate scenarios involving BDS-3, GPS, and dual-system settings, we systematically validate the efficacy of the method. The experimental results indicate that the convergence time of the method is less than 4 min in a single-system scenario. Furthermore, in a dual-system scenario, the method can achieve rapid convergence in less than 3 min. The CZS-PPP technique presented demonstrates the elimination of integer ambiguities and the effective suppression of system residuals, in comparison to the conventional method. The proposed approach has demonstrated remarkable performance across different systems, offering a promising new pathway for achieving PPP fast convergence in BDS/GNSS.

Keyword Precise point positioning, Rapid convergence, Doppler principle, Zero-baseline self-differencing

For over 30 years, the development of PPP has progressed slowly. The lengthy convergence time of PPP has posed an international challenge, impeding its adoption in the scientific, academic, and industrial communities and preventing its real-time and commercial use. To address the issue of shortening PPP convergence time effectively, international scholars have proposed several classic PPP models, including the Single-Difference (SD) model^{1,2}, the Uncombined (UC) positioning model³, the University of Calgary model (UoFC)⁴, and the ionosphere-free combination model (IF)^{5–8}. In recent years, with the development of BeiDou Navigation Satellite System (BDS) and Galileo, research on PPP using multi-frequency, multi-system, and multi-frequency multi-system combinations has become a hot topic.

BDS-3 was the first to launch onboard real-time PPP services internationally. Researchers such as Zhang et al. evaluated the static and dynamic positioning performance of PPP-B2b⁹. For BDS-3 (BDS-3 + GPS), the static positioning accuracy was 2.6 (2.1) cm, the dynamic positioning accuracy was 21.5 (15.2) cm horizontally and 33.4 (30.3) cm vertically, with a convergence time of 17.4 (16.2) minutes. Other scholars have reported similar performance results^{10–13}. Multi-frequency combination models are advantageous for speeding up PPP convergence¹⁴. Duong V analyzed the UD model, showing that its convergence time could reach 15 min with positioning accuracy better than 10 cm¹⁵. Laurichesse D analyzed the positioning performance of three-frequency PPP, demonstrating centimeter-level accuracy¹⁶. Academician Yang Yuanxi, Basile F, Zhang Xiaohong, and others analyzed the convergence performance of three-frequency PPP. The experimental results indicate that the convergence time of three-frequency PPP can be shortened to 10 minutes^{17–19}.

¹School of Mathematics and Computational Science, Xiangtan University, Xiangtan 411105, Hunan, China. ²School of Automation and Electronic Information, Xiangtan University, Xiangtan 411105, Hunan, China. ³School of Materials Science and Engineering, Xiangtan University, Xiangtan 411105, Hunan, China. ⁴Shanghai Astronomical Observatory, Chinese Academy of Sciences, Shanghai 200030, China. ⁵School of Physical Science and Technology, ShanghaiTech University, Shanghai 200030, China. ✉email: chengcailin@126.com; lkh8022150@gmail.com

Multi-system combination models also play a significant role in accelerating PPP convergence²⁰. The primary benefit of employing multi-system combination lies in the increased number of observed satellites and improved spatial geometry, resulting in enhanced PPP convergence time and positioning accuracy. Noteworthy researchers such as Geng Jianghui, Li Xingxing, and Duong V. have delved into the study of multi-system PPP models, demonstrating that, in comparison to single-system models, multi-system PPP models have the capability to expedite the resolution of integer ambiguities^{21,22}. In another exploration, Zhang Baocheng, Li Xingxing, and their colleagues investigated the GCRE four-system PPP model and determined that the static convergence time for the four-system PPP model could be reduced to less than 10 min, with positioning accuracy better than 10 cm²³. Furthermore, the multi-frequency multi-system combination model has also attracted great attention. The results show that the combination of multi-frequency and multi-system can further shorten the convergence time²⁴. In conclusion, diverse combination models can significantly reduce PPP convergence time, albeit facing constraints such as errors in atmospheric delay models, time-varying effects, and gradual changes in GNSS satellite constellations.

In recent years, two new PPP mechanisms, Precise Point Positioning and Real-Time Kinematic (PPP-RTK) and Low Earth Orbit Satellite Navigation Enhanced GNSS (LE-GNSS), have gained significant attention. PPP-RTK aims to overcome the factors impeding rapid convergence in PPP, with a primary focus on effectively resolving errors in atmospheric delay models and their temporal variations²⁵. Introduced by Germany's Wübbena in 2005, this concept relies on ground-based CORS networks to accurately differentiate satellite orbits, satellite clock errors, and atmospheric delay errors. Users can leverage this model data to achieve instantaneous centimeter-level positioning, akin to Real-Time Kinematic (RTK)^{26–28}. The “Heavenly RTK” proposed by Hexagon in the United States, essentially disseminates this data via satellites, rendering it a satellite-based PPP-RTK technology. LE-GNSS addresses the slow-changing GNSS satellite constellation structure. Low Earth Orbit (LEO) satellites operate at high speeds, and when combined with BDS-3, they can rapidly alter the geometric structure of GNSS navigation constellations. This approach can solve the ill-posed problem of multi-epoch combined PPP models in a short time frame. Researchers like Li Bofeng and Li Xingxing have conducted studies and analysis, suggesting preliminary conclusions that, with a sufficient number of deployed LEO satellites (300 or more), LE-GNSS can achieve PPP convergence times of less than 1 minute^{29,30}.

Harnessing external aids, such as Heavenly RTK and LEO Satellite Navigation Enhancement, undeniably contributes to overcoming the international challenge of PPP slow convergence. This paper seeks to investigate whether PPP can achieve swift convergence autonomously, without relying on external assistance.

Principles and methods

CZS-PPP principle

The core principle entails employing itself as a reference, essentially considering the epochs before and after as the reference station and the mobile station. This involves a static baseline length of zero and a dynamic baseline length approaching zero, forming a zero-baseline self-differencing mode. Changes in position relative to the previous epoch are computed by analyzing the carrier phase variations between the current and preceding epochs. This involves subtracting the carrier phase from the previous epoch from the carrier phase of the current epoch. Subsequently, the self-differencing values for carrier phase at each frequency are calculated. The coordinates are then determined using a dual-frequency ionosphere-free combination model.

The basic procedure of our method is as follows: In the first step, Single-Point Positioning (SPP) is used to determine the receiver coordinates at the initial epoch. In the second step, taking the receiver coordinates at the initial epoch as a virtual station, epoch differencing is performed between the second epoch and the initial epoch. The solution provides the coordinate changes relative to the virtual station, so the receiver coordinates at the second epoch are obtained by adding the virtual station coordinates and the coordinate changes. In the third step, the virtual station is updated, taking the receiver coordinates at the second epoch as the new virtual station. Similarly, epoch differencing is performed between the third epoch and the second epoch to obtain new coordinate changes and the receiver coordinates at the third epoch, updating the virtual station. This process is iteratively applied to subsequent epochs until convergence to the true receiver coordinates is achieved. The carrier phase observation equation (converted to distance), as shown in the equation, is used.

$$L_i = \rho + c \cdot \delta t_k - c \cdot \delta t^j + G_h \cdot T_h + G_w \cdot T_w - I_i + N_i + \varepsilon_{L_i} \quad (1)$$

In the above equation, L_i represents the carrier phase observations (converted to distance), where the subscript i denotes the carrier frequency. ρ is the satellite-to-ground geometric distance, δt_k represents the receiver clock bias, δt^j represents the satellite clock bias, and c is the speed of light, all in units of seconds. G_h and G_w are the tropospheric zenith direction dry and wet mapping functions, respectively. T_h represents the zenith direction dry delay component, obtained from the Saastamoinen model³¹. T_w represents the zenith direction wet delay component and is treated as an estimated parameter alongside position parameters. I_i represents the ionospheric delay on L_i . ε_{L_i} represents the observation noise for carrier phase, all in units of meters. N_i represents the integer ambiguity on L_i .

The Eq. (1) is differenced between consecutive epochs to obtain the zero-baseline self-differencing equation (converted to distance) as follows:

$$\Delta L_i = L_t - L_{t-1} = \Delta \rho + c \cdot (\Delta \delta t_k - \Delta \delta t^j) + G_h \cdot \Delta T_h + G_w \cdot \Delta T_w - \Delta I_i + \Delta \varepsilon_{L_i} \quad (2)$$

In the equation, Δ represents the differencing operator between consecutive epochs. The carrier phase zero-baseline self-differencing eliminates the integer ambiguity parameters. $\Delta \rho$ represents the change in satellite-to-receiver geometric distance between consecutive epochs, and $\Delta \rho$ is defined as follows:

$$\Delta\rho = \rho_t - \rho_{t-1} = e_t \cdot (R_t^s - R_t^r) - e_{t-1} \cdot (R_{t-1}^s - R_{t-1}^r) \tag{3}$$

In the equation, t and $t - 1$ represent two consecutive epochs; $e_t = \frac{R_t^s - R_t^r}{|R_t^s - R_t^r|}$ represents the unit direction vector from the receiver to the satellite; R_t^s represents the satellite coordinate vector, and R_t^r represents the receiver coordinate vector. Additionally, $R_t^r = R_{t-1}^r + \Delta R$, where ΔR represents the change in receiver coordinates. Therefore, $\Delta\rho$ can be expressed as follows:

$$\Delta\rho = -e_t \cdot \Delta R + e_t \cdot (R_t^s - R_{t-1}^r) - e_{t-1} \cdot (R_{t-1}^s - R_{t-1}^r) \tag{4}$$

Substituting Eq. (4) into Eq. (2) yields:

$$\begin{aligned} \Delta L_i = & -e_t \cdot \Delta R + e_t \cdot (R_t^s - R_{t-1}^r) - e_{t-1} \cdot (R_{t-1}^s - R_{t-1}^r) + c \cdot (\Delta\delta t_k - \Delta\delta t^j) \\ & + G_h \cdot \Delta T_h + G_w \cdot \Delta T_w - \Delta I_i + \Delta\varepsilon_{L_i} \end{aligned} \tag{5}$$

and calculate its error equation as:

$$v = [-e_x - e_y - e_z 1 G_w] \cdot \begin{bmatrix} \Delta x \\ \Delta y \\ \Delta z \\ c \cdot \Delta\delta t_k \\ \Delta T_w \end{bmatrix} - l \tag{6}$$

where l is:

$$e_t = (e_x, e_y, e_z) = \left(\frac{X^J - X_K^0}{|R_t^s - R_t^r|}, \frac{Y^J - Y_K^0}{|R_t^s - R_t^r|}, \frac{Z^J - Z_K^0}{|R_t^s - R_t^r|} \right) \tag{7}$$

(X^J, Y^J, Z^J) represents the satellite coordinates, while (X_K^0, Y_K^0, Z_K^0) represents the approximate coordinates of the receiver.

$$\Delta R = (\Delta x, \Delta y, \Delta z) \tag{8}$$

$$l = \Delta L_i - e_t \cdot (R_t^s - R_{t-1}^r) + e_{t-1} \cdot (R_{t-1}^s - R_{t-1}^r) + c \cdot \Delta\delta t^j - G_h \cdot \Delta T_h + \Delta I_i \tag{9}$$

In Eqs. (6), v represents the residual vector, l denotes the known parameters, and the parameters to be estimated include the changes in receiver coordinates ΔR for both before and after epochs, the variation in tropospheric zenith wet delay component ΔT_w , and the receiver clock bias change $\Delta\delta t_k$. When a sufficient number of visible satellites is available, these parameters can be estimated through the least-squares method or Kalman filtering.

Reconstructed Doppler method

Presently, the unprocessed Doppler observations obtained from receivers display substantial noise, making them unsuitable for accurate GNSS positioning or velocity estimation due to elevated error levels and diminished accuracy. As a result, a method has been suggested to reconstruct Doppler frequency shift values, aiming to produce noise-free theoretical values. The reconstructed alterations in carrier phase demonstrate remarkable precision and are devoid of cycle slips.

The reconstructed Doppler frequency shift values depend on various parameters, such as satellite positions, satellite clock biases, tropospheric delays, ionospheric delays, receiver velocity, receiver position, and receiver clock biases, among others. These parameters constitute the variables to be estimated, establishing a theoretical basis for the pseudorange single-point positioning model utilizing reconstructed Doppler values.

For satellite positioning, satellites orbit around the Earth, making them mobile signal sources. When extending the formula to single-point positioning, one can derive the reconstructed Doppler frequency shift value, denoted as f_d . In Fig. 1, the observation vector $\vec{\rho}$ of a satellite points from the receiver to the satellite, while the \vec{v} vector represents the receiver's velocity. Let $\vec{v}_s = (x_{vs}, y_{vs}, z_{vs})$ be the satellite velocity, $P_s = (x_s, y_s, z_s)$ be the satellite position, and $P_u = (x_u, y_u, z_u)$ be the receiver's position, obtained through pseudorange positioning. Therefore, $\vec{\rho} = (x_\rho, y_\rho, z_\rho) = (x_s - x_u, y_s - y_u, z_s - z_u)$. The reconstructed Doppler value can be calculated as follows:

$$f_d = \frac{(\vec{v} - \vec{v}_s) \cdot \vec{l}}{\lambda} \tag{10}$$

In the equation, \vec{l} is the unit observation vector, $\vec{l} = \vec{\rho}/|\vec{\rho}|$, where $|\vec{\rho}|$ represents the satellite-to-earth geometric distance, λ is the wavelength. The dot symbol “ \cdot ” denotes vector dot product.

Due to the presence of cycle slips, clock jumps, and gross errors in traditional carrier phase-smoothed pseudorange methods, this paper introduces a method to calculate the carrier phase change quantity $\lambda \cdot \Delta\Phi_{ij}$ (converted to distance) through the integration of the reconstructed Doppler frequency shift values. This method can be expressed as follows:

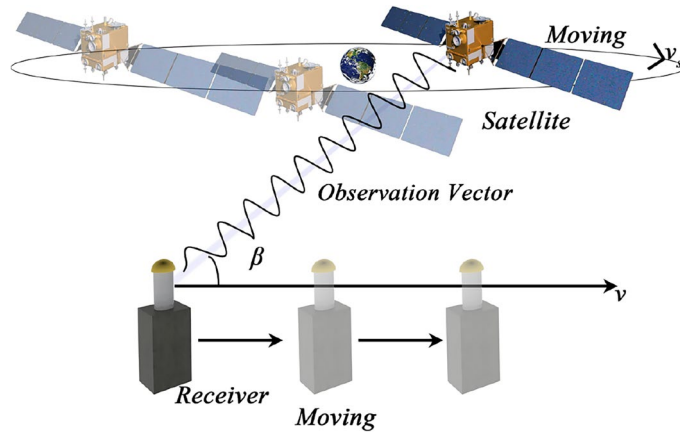


Figure 1. Doppler model of satellites and receivers.

$$\lambda \cdot \Delta\Phi_{ij} = \lambda(\Phi_j - \Phi_i) = \lambda \int_{t_i}^{t_j} f_d dt \tag{11}$$

In the equation, λ represents the wavelength of the carrier signal transmitted by the satellite, t_i and t_j are two epochs in time, $f_d(t_i)$ and $f_d(t_j)$ represent the reconstructed Doppler frequency shift values at the two epochs, Φ_i and Φ_j denote the carrier phase observations at the two epochs, and $\lambda \cdot \Delta\Phi_{ij}$ represents the carrier phase change between the two epochs. The time difference between t_j and t_i represents the time interval between the two epochs. This approach effectively mitigates the effects of carrier phase observations including cycle slips, clock jumps, and gross errors.

Moreover, considering the carrier phase change between epochs as an indicator of the pseudorange rate, and in an ideal scenario where factors like ionospheric effects, tropospheric effects, and receiver clock bias are disregarded, the theoretical equivalence of pseudorange change and carrier phase change between the same epochs holds true. Nevertheless, in real-world scenarios, owing to diverse errors and observational noise, the carrier phase change exhibits greater precision compared to the pseudorange change. Consequently, incorporating the reconstructed Doppler frequency shift values to substitute the pseudorange change can result in a more smoothed pseudorange and enhanced pseudorange accuracy, as outlined below:

$$\delta\rho^j(t_i, t_j) = \lambda \cdot \Delta\Phi_{ij} = \lambda \int_{t_i}^{t_j} f_d dt \tag{12}$$

In the equation, $\delta\rho^j(t_i, t_j)$ represents the change in pseudorange between two epochs, t_i and t_j .

The initial epoch positioning relies on single-point pseudorange positioning, where pseudorange measurements are susceptible to significant noise. This noise is a random variable conforming to a zero-mean normal distribution, typically ranging between 5 and 10 m. Consequently, mitigating pseudorange noise becomes imperative. While traditional carrier phase-smoothed pseudorange techniques³² with Doppler observations show no signs of cycle slips, Doppler observations from GNSS receivers often harbor considerable noise, leading to heightened errors and diminished accuracy. In light of this, a novel approach based on reconstructed Doppler for carrier phase-smoothed pseudorange is proposed to effectively suppress pseudorange noise and enhance accuracy. The underlying principle of this method is elucidated below:

The pseudorange observations at the first epoch can be deduced by integrating the carrier phase change quantities obtained from different epochs' reconstructed Doppler values. A smoothing window of length k is defined, which means there are k observations within the window: $\rho^j(t_1), \rho^j(t_2), \dots, \rho^j(t_k)$. By utilizing the integrated reconstructed Doppler frequency shift values, carrier phase change quantities $\delta\rho^j(t_1, t_2), \delta\rho^j(t_1, t_3), \dots, \delta\rho^j(t_1, t_k)$ can be calculated from t_1 to t_k and retroactively applied to the first epoch. Consequently, k pseudorange observations are available for the first epoch, namely:

$$\begin{aligned} \rho^j(t_1)_1 &= \rho^j(t_1) \\ \rho^j(t_1)_2 &= \rho^j(t_2) - \delta\rho^j(t_1, t_2) = \rho^j(t_2) - \lambda \int_{t_1}^{t_2} f_d dt \\ &\dots\dots \\ \rho^j(t_1)_k &= \rho^j(t_k) - \delta\rho^j(t_1, t_k) = \rho^j(t_k) - \lambda \int_{t_1}^{t_k} f_d dt \end{aligned} \tag{13}$$

As the sliding window encompasses k epochs, the pseudorange values computed for these k epochs are averaged to derive the smoothed pseudorange value for the initial epoch:

$$\overline{\rho^j(t_1)} = \frac{1}{k} \sum_{i=1}^k \rho^j(t_1)_i \quad (14)$$

By leveraging the integrated Doppler frequency shift values reconstructed at any specific epoch, it is possible to calculate the alteration in pseudorange concerning the initial epoch time. Following this, through the process of smoothing and adjusting the mean pseudorange value at the initial epoch time, one can obtain smoothed pseudorange values for all subsequent epochs.

$$\overline{\rho^j(t_i)} = \overline{\rho^j(t_1)} + \delta\rho^j(t_1, t_i) = \overline{\rho^j(t_1)} + \lambda \int_{t_1}^{t_i} f_d d \quad (15)$$

First, we integrate the Doppler values, and then obtain the integrated change by subtracting the values between consecutive epochs. This integrated change reflects the variation in noise. In Fig. 2, the comparison shows the difference between reconstructed Doppler values and Doppler observations (generated by the receiver observation file): Reconstructed Doppler values are smooth and noise-free, with a monotonically increasing curve reflecting the relative motion trajectory between the satellite and the receiver. In contrast, Doppler observation values are mixed with observational noise, displaying irregular and non-stationary fluctuations.

Figure 3 compares the original pseudorange observations with the pseudorange observations smoothed by reconstructed Doppler. The positioning performance of these two types of observations is further validated in Fig. 4. It can be observed from Fig. 4 that the SPP-Reconstruct Doppler (the SPP with Reconstructed Doppler smoothed pseudorange) demonstrates significantly better positioning accuracy and stability compared to SPP with original pseudorange observations.

CZS-PPP ionosphere-free combination model

The conventional PPP method employs the dual-frequency ionosphere-free model (PPP-IF), where the combined model of pseudorange and carrier phase observations is as follows:

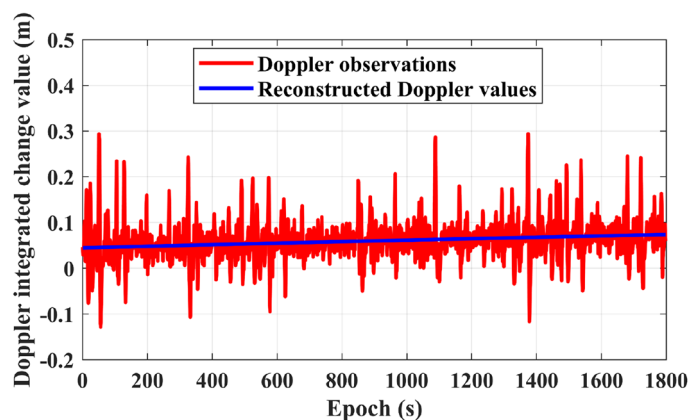


Figure 2. Comparison of the integrated changes between observed Doppler values and reconstructed Doppler values.

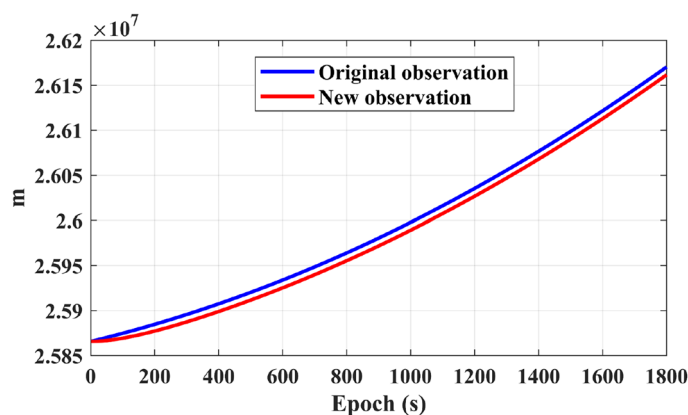


Figure 3. Comparison between original observations and newly generated observations.

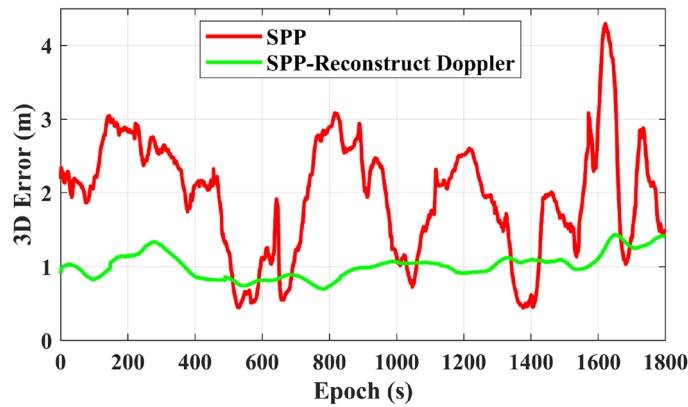


Figure 4. Comparison of three-dimensional positioning errors between SPP and SPP-reconstruct doppler.

$$P_{IF} = \frac{f_1^2 P_1 - f_2^2 P_2}{f_1^2 - f_2^2} = \rho + c \cdot (\delta t_k - \delta t^j) + G_h \cdot T_h + G_w \cdot T_w + \varepsilon_{P_{IF}} \tag{16}$$

$$L_{IF} = \frac{f_1^2 L_1 - f_2^2 L_2}{f_1^2 - f_2^2} = \rho + c \cdot (\delta t_k - \delta t^j) + G_h \cdot T_h + G_w \cdot T_w + \lambda_{IF} \cdot N_{IF} + \varepsilon_{L_{IF}} \tag{17}$$

In eqs. (16) and (17), P_{IF} represents the ionosphere-free combined observations of dual-frequency pseudorange observations P_1 and P_2 ; L_{IF} represents the ionosphere-free combined observations of dual-frequency carrier phase observations L_1 and L_2 ; f_1 and f_2 are the frequencies of the observations; δt_k denotes the receiver clock bias; δt^j represents the satellite clock bias; c is the speed of light in vacuum; G_h and G_w are the mapping functions for dry and wet tropospheric delays, respectively; T_h and T_w are the dry and wet tropospheric delays; N_{IF} is the integer ambiguity of the ionosphere-free combined carrier phase observations; λ_{IF} is the wavelength of the ionosphere-free combined observations; $\varepsilon_{P_{IF}}$ and $\varepsilon_{L_{IF}}$ denote the noise errors of the pseudorange and carrier phase observations, respectively.

The dual-frequency ionosphere-free combination model³³ for CZS-PPP is presented as follows:

$$P_{IF} = \frac{f_1^2 P_1 - f_2^2 P_2}{f_1^2 - f_2^2} = \rho + c \cdot (\delta t_k - \delta t^j) + G_h \cdot T_h + G_w \cdot T_w + \varepsilon_{P_{IF}} \tag{18}$$

$$\Delta L_{IF} = \frac{f_1^2 \cdot L_1 - f_2^2 \cdot L_2}{f_1^2 - f_2^2} = \Delta \rho + c \cdot (\Delta \delta t_k - \Delta \delta t^j) + G_h \cdot \Delta T_h + G_w \cdot \Delta T_w + \Delta \varepsilon_{L_{IF}} \tag{19}$$

In Eqs. (18) and (19), P_{IF} and ΔL_{IF} represent the ionosphere-free linear combinations of pseudorange observations and carrier phase self-differencing values on BDS-3 satellites B1C and B2A, respectively. ρ is the geometric distance from the receiver to the satellite, and $\Delta \rho$ represents the change in satellite-to-receiver geometric distance between the previous and current epochs. G_h and G_w are the tropospheric zenith direction dry and wet mapping functions, respectively. ΔT_h is the change in tropospheric zenith direction dry delay component between the previous and current epochs, and ΔT_w is the change in tropospheric zenith direction wet delay component between the previous and current epochs. ΔT_w is treated as an estimated parameter along with position parameters. $\varepsilon_{P_{IF}}$ represents the pseudorange observation noise for the ionosphere-free combination, while $\Delta \varepsilon_{L_{IF}}$ represents the phase observation noise for the ionosphere-free combination between the previous and current epochs. All the above units are in meters. c denotes the speed of light. $\Delta \delta t_k$ is the change in receiver clock bias between the previous and current epochs, and $\Delta \delta t^j$ is the change in satellite clock bias between the previous and current epochs, both in seconds. Other error terms in the observation equation (such as antenna phase center corrections³⁴, phase wind-up effects³⁵, tidal loading deformations³⁶, relativistic effects³⁷, and Earth rotation³⁸) are corrected using respective models. The dual-frequency ionosphere-free combination model offers the advantages of eliminating first-order ionospheric effects with fewer estimated parameters, resulting in stable positioning performance, a simple model, and ease of operation.

In our research, we utilized L_1 and L_2 dual-frequency observations from the BDS-3 and GPS dual-systems³⁹ to compute the intermediate-frequency combinations. The ionosphere-free combination equation, established based on pseudorange observations and carrier phase self-differencing values, can be expressed as:

$$P_{IF}^g = \rho^g + c \cdot \delta t_k + G_w \cdot T_w^g + \varepsilon_{P_{IF}}^g \tag{20}$$

$$\Delta L_{IF}^g = \Delta \rho^g + c \cdot \Delta \delta t_k + G_w \cdot \Delta T_w^g + \Delta \varepsilon_{L_{IF}}^g \tag{21}$$

$$P_{IF}^b = \rho^b + c \cdot \delta t_k + G_w \cdot T_w^b + c \cdot \delta t_{sys}^{b,g} + \varepsilon_{PIF}^b \quad (22)$$

$$\Delta L_{IF}^b = \Delta \rho^b + c \cdot \Delta \delta t_k + G_w \cdot \Delta T_w^b + c \cdot \Delta \delta t_{sys}^{b,g} + \Delta \varepsilon_{LIF}^b \quad (23)$$

In the equations, Δ represents the differencing operator between the previous and current epochs. The superscripts g and b denote GPS and BDS-3 satellites, respectively. $\delta t_{sys}^{b,g}$ represents the system time difference parameter between GPS and BDS-3, measured in seconds. In the dual-constellation PPP model combining GPS and BDS-3, in this paper, GPS time is used as the reference and BDS-3 time is converted to GPS time. In addition, we include the parameter $\delta t_{sys}^{b,g}$ in the set of parameters to be determined for estimating the system clock difference between GPS and BDS-3. The dual-frequency ionosphere-free combination model consists of five parameters: position changes ($\Delta x, \Delta y, \Delta z$), receiver clock bias $\Delta \delta t_k$, tropospheric zenith wet component ΔT_w , and system time difference parameter $\delta t_{sys}^{b,g}$.

$$dX = \left[\Delta x, \Delta y, \Delta z, \Delta \delta t_k, \Delta T_w, \Delta \delta t_{sys}^{b,g} \right] \quad (24)$$

In this paper, a conventional random model is used, and the noise (σ) in the observation equation is weighted according to the elevation angle.

$$\begin{cases} \sigma(ele) = \sigma_0 & ele > 30^\circ \\ \sigma(ele) = \frac{\sigma_0}{2 \sin(ele)} & else \end{cases} \quad (25)$$

In the Eq. (25), ele is the elevation angle. σ_0 is commonly set to 1 m for pseudorange observations and 1 cm for phase observations. The random model is as follows:

$$w = R^{-1} = \begin{bmatrix} \frac{1}{\sigma_1^2} & & & \\ & \ddots & & \\ & & \ddots & \\ & & & \frac{1}{\sigma_n^2} \end{bmatrix} \quad (26)$$

In the Eq. (26), w signifies the weight matrix of the observations, while R denotes the covariance matrix associated with the observations.

Due to the different observation accuracies of GPS and BDS, the corresponding observation weights are also different. In this paper the observation weights of GPS and BDS are set to 1:2.

Algorithm validation and performance analysis

The method in this paper is applicable to static mode, in order to verify the effectiveness of the above CZS-PPP algorithm for static data processing, experiments will be carried out utilizing a Beidou Xingtong receiver at the Intelligent Navigation and Remote Sensing Research Center of Xiangtan University. All receivers employed in these experiments will utilize both the GPS and BDS-3 satellite navigation systems for precise positioning.

As depicted in Fig. 5, the algorithmic experiments employed a dual-frequency GNSS receiver (BeiDou Xingtong) positioned on the rooftop of the Information Building at Xiangtan University to capture satellite signals.

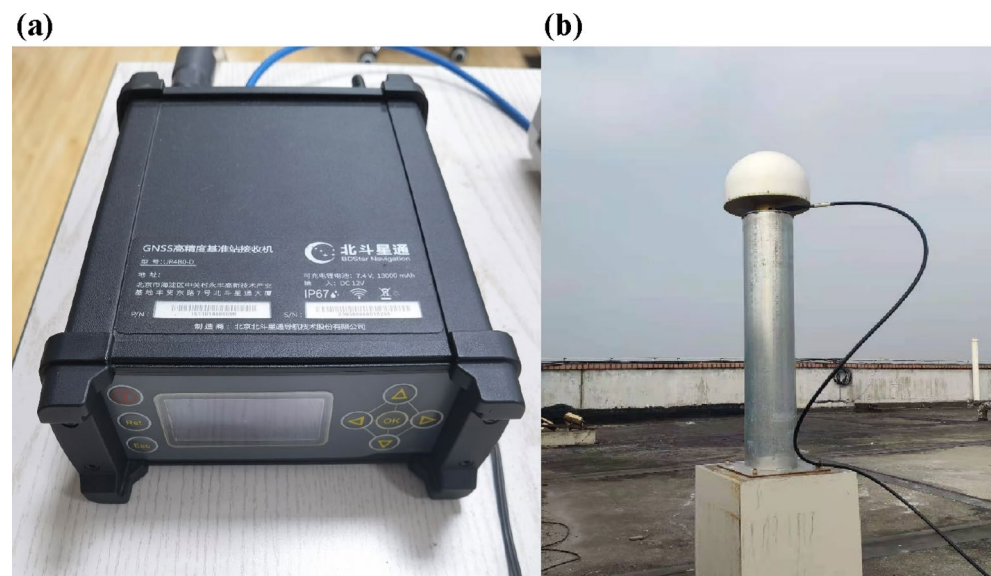


Figure 5. (a) Beidou Xingtong Receiver and (b) Beidou Xingtong Antenna.

This setup significantly reduced multipath effects, which could be considered negligible. The Earth Centered, Earth Fixed (ECEF) coordinates of its antenna were accurately measured using standard precision instruments, achieving an accuracy better than 3 mm. Original observation data spanning days 017–023 of the year 2023, totaling 7 days, was acquired. The data was sampled at 1-s intervals, encompassing simultaneous reception of BDS-3 and GPS satellite data. Raw observation data was collected daily from 9:00 to 10:00, over a one-hour period. The convergence criteria in this paper are as follows: achieving convergence thresholds simultaneously in the East (E), North (N), and Up (U) directions for PPP, and ensuring stability within the thresholds for 120 consecutive epochs (with a sampling interval of 60 min). The convergence threshold is set at 10 cm, and the convergence time is measured from the initial epoch to reaching the convergence threshold. The experiment utilized dual-frequency raw observation data from BDS-3 and GPS satellite systems to validate the superiority of CZS-PPP.

Experiment 1

In conditions where only a single system was considered, distinct experiments were conducted to validate and compare the individual BDS-3 system^{40,41} and the standalone GPS system. Precise satellite coordinates and accurate satellite clock biases were sourced from products provided by the International GNSS Service (IGS) center. CZS-PPP utilized 5-min precise satellite coordinates and 30-s precise satellite clock bias products from the German Research Centre for Geosciences (GFZ). Raw observations in dual frequency, encompassing BDS-3 B1C, B2A^{42,43}, and GPS L1C, L2W, were collected over seven consecutive days, from the 17th to the 23rd day of the year 2023, as acquired by the receiver.

Figure 6 showcases the positioning results for a single BDS-3 system. In the diagram, (E, N, U) represent a specific station coordinate system, known as the East-North-Up (ENU) coordinate system. The ENU coordinate system captures the positional changes of the receiver in the East (E), North (N), and Up (U) directions. The error curves in the figure depict the absolute differences between the coordinates obtained through CZS-PPP calculations and the receiver's standard coordinates in the ENU coordinate systems. Over time, convergence is achieved. At 217 s, the convergence reaches 0.07 m in the E direction, 0.06 m in the N direction, and 0.08 m in the U direction. Figure 7 illustrates the number of BDS-3 satellites observed within an hour. During the specified time interval, approximately 8 satellites are observed, meeting the minimum requirement of at least 4 satellites for positioning.

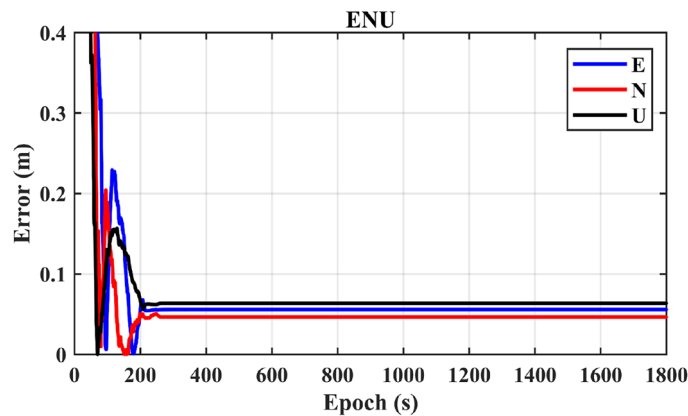


Figure 6. Positioning results for a single BDS-3 system.

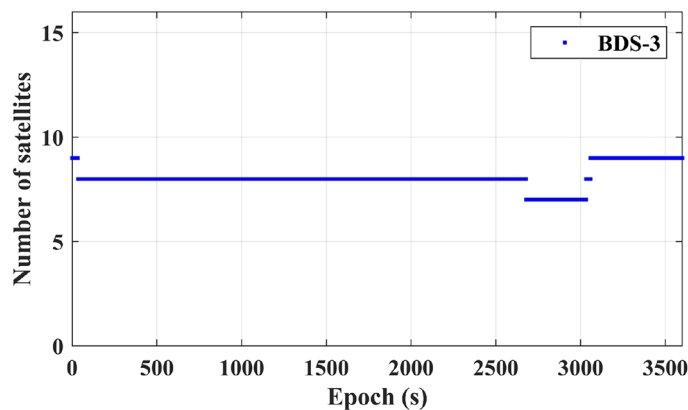


Figure 7. BDS-3 satellite observations.

Figure 8 depicts the positioning results for a single GPS system. Over time, convergence is attained, reaching 0.03 m in the E direction, 0.08 m in the N direction, and 0.09 m in the U direction at 201 s. Following convergence, the positioning accuracy remains consistently stable. In contrast, Fig. 9 illustrates that the number of GPS satellites is approximately equivalent to the number of BDS-3 satellites.

Table 1 presents information on the convergence time and three-dimensional RMS positioning accuracy in the ENU coordinates for both the individual BDS-3 satellite system and the standalone GPS satellite system. Based on continuous observations spanning 7 days, it is evident that the average convergence time for the single BDS-3 system is 220 s, accompanied by an average ENU three-dimensional RMS positioning accuracy of 0.08 m. In comparison, the single GPS system demonstrates an average convergence time of 214 s, with an average ENU three-dimensional RMS positioning accuracy of 0.076 m. The two satellite systems display comparable average convergence times and average positioning accuracy.

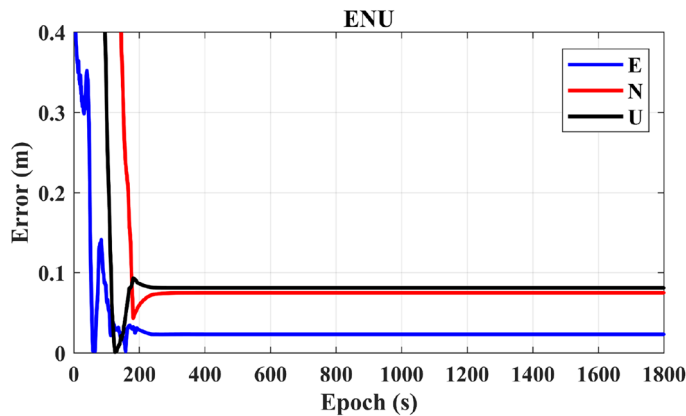


Figure 8. Presents the positioning results for a single GPS system.

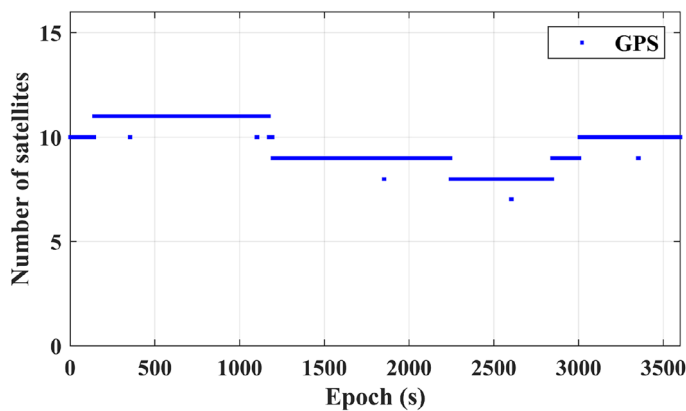


Figure 9. Displays the number of observed GPS satellites.

Statistic (Annual date)	BDS-3		GPS	
	Convergence(s) RMS(m)	ENU 3D	Convergence(s) RMS(m)	ENU 3D
017	213	0.08	201	0.07
018	229	0.09	200	0.10
019	205	0.07	219	0.06
020	233	0.10	213	0.10
021	223	0.10	198	0.05
022	225	0.05	237	0.08
023	217	0.07	221	0.07
Mean	220	0.08	214	0.076

Table 1. Comparison between BDS-3 and GPS systems.

Experiment 2

In the context of the BDS-3/GPS dual-satellite system^{44,45}, the positioning results of CZS-PPP are compared with those of the widely employed PPP method. The conventional PPP method employs the PPP-IF model^{46,47}. Both methodologies utilize identical observational data and precise ephemeris. A comparative analysis is conducted using data continuously collected for 7 days, drawn from the dual-frequency raw data received by the receiver over the consecutive 7 days, spanning from day 17 to day 23 in 2023.

In Fig. 10, in the context of a dual-satellite navigation system, a notable increase in the count of visible satellites is depicted, leading to an enhanced satellite spatial geometry.

In Fig. 11, it is evident that the convergence time for PPP-IF is notably extended, requiring approximately 700 s to converge, and achieving a three-dimensional average positioning accuracy of 0.15 m.

The outcomes illustrated in Fig. 12 clearly demonstrate the superior performance of CZS-PPP over PPP-IF. CZS-PPP achieves convergence in 152 s and sustains a three-dimensional average positioning accuracy of 0.06 m. This highlights the superior performance of CZS-PPP in terms of both convergence time and positioning accuracy when compared to PPP-IF.

In Fig. 13, this paper presents a statistical comparison of the system residual errors between CZS-PPP and the traditional PPP-IF method under the dual-constellation conditions of GPS and BDS-3. The horizontal axis represents satellite numbers, and the vertical axis represents system residual errors. It can be observed that the system residual errors of the proposed method are significantly smaller than those of the traditional PPP-IF method.

Table 2 presents data spanning seven consecutive days. The average convergence time for PPP-IF is 709 s, accompanied by an average three-dimensional RMS positioning accuracy of 0.132 m. In contrast, CZS-PPP attains an average convergence time of 156 s, with an average three-dimensional RMS positioning accuracy of 0.068 m. This underscores the superior performance of CZS-PPP.

Conclusions

This study delves into the critical factors impeding the rapid convergence of PPP, such as integer ambiguity and residual errors within the system. Notably, it addresses these challenges without relying on external sources like ground augmentation networks or enhancements from low Earth orbit satellite navigation systems, resulting in a significant reduction in PPP convergence time. The proposed method, termed Carrier Phase Zero-Baseline Self-Differencing PPP (CZS-PPP), initially employs principles of satellite precise orbits and Doppler generation

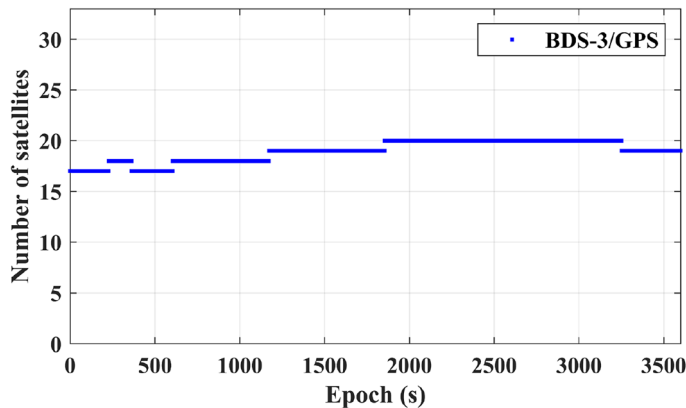


Figure 10. Number of BDS-3/GPS dual-system satellite observations.

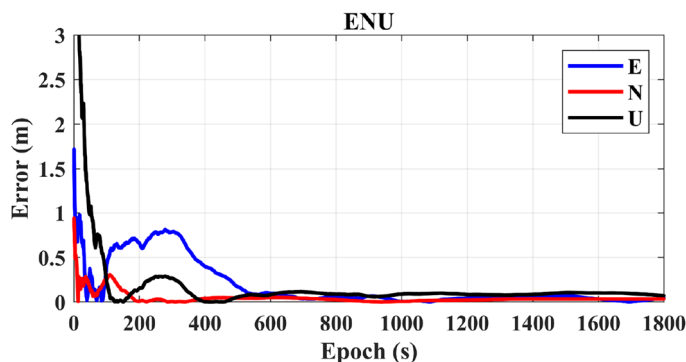


Figure 11. PPP-IF positioning results.

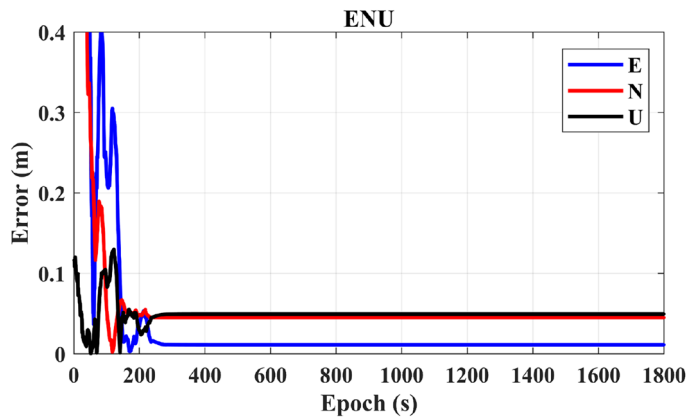


Figure 12. Positioning results of CZS-PPP.

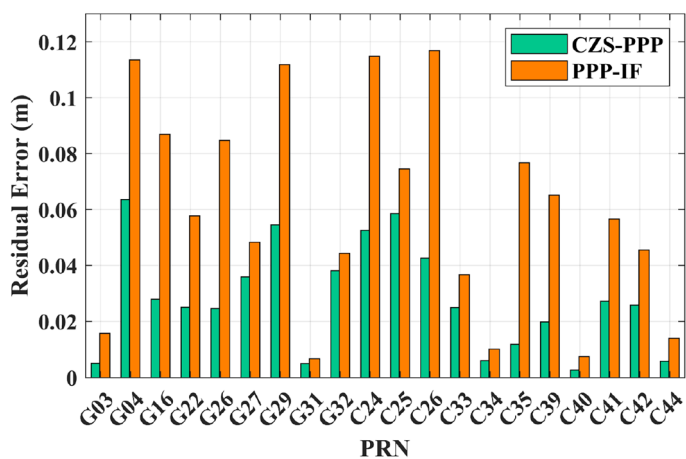


Figure 13. Comparison of system residual errors between CZS-PPP and PPP-IF.

Statistic (Annual date)	PPP-IF		CZS-PPP	
	Convergence(s) RMS(m)	ENU 3D	Convergence(s) RMS(m)	ENU 3D
017	688	0.11	147	0.05
018	732	0.16	168	0.09
019	714	0.10	159	0.05
020	722	0.12	162	0.06
021	700	0.15	152	0.07
022	681	0.12	143	0.06
023	729	0.17	165	0.10
Mean	709	0.132	156	0.068

Table 2. Comparison between CZS-PPP and PPP-IF.

to reconstruct error-free Doppler measurements. It then utilizes Doppler integration equations to smooth pseudorange, minimizing cumulative residual errors and enhancing pseudorange accuracy for precise initial epoch coordinates. Subsequently, through self-differencing between consecutive epochs, system residual errors and integer ambiguities are further mitigated, leading to a substantial reduction in PPP convergence time. The single-system case achieves convergence in less than 4 min, while the dual-system case converges in under 3 min. The accuracy of these findings is effectively validated using actual measurements from BDS-3, GPS, and BDS-3/GPS. This research contributes crucial theoretical and technical support for real-world applications of BDS-3/GNSS real-time PPP.

Data availability

The data related to or connected with the work are all encompassed in the manuscript and its supporting information. The datasets generated and/or analysed during the current study are not publicly available due the confidentiality of this project but are available from the corresponding author on reasonable request.

Received: 7 November 2023; Accepted: 30 May 2024

Published online: 01 June 2024

References

1. Elsobeiy, M. & El-Rabbany, A. Efficient between-satellite single-difference precise point positioning model. *J. Surv. Eng.* **140**(2), 04014007 (2014).
2. Afifi, A. & El-Rabbany, A. Improved between-satellite single-difference precise point positioning model using triple GNSS constellations: GPS, Galileo, and BeiDou. *Positioning* **7**(2), 63–74 (2016).
3. Zhao, Q. *et al.* Multi-GNSS fast precise point positioning with multi-frequency uncombined model and cascading ambiguity resolution. *Math. Probl. Eng.* **2022**, 1–16 (2022).
4. Zangenehjad, F., Gao, Y. Application of UofC model based multi-GNSS PPP to smartphones GNSS positioning. In: proceedings of the 34th international technical meeting of the satellite division of the institute of navigation (ION GNSS+ 2021). 2021: 2986–3003.
5. Odijk, D. Ionosphere-free phase combinations for modernized GPS. *J. Surv. Eng.* **129**(4), 165–173 (2003).
6. Srinivas, V.S., Yedukondalu, K. Code-phase based combined GPS-Galileo positioning using Ionosphere-free linear combination//2019 URSI Asia-Pacific Radio Science Conference (AP-RASC). IEEE, 2019: 1–4.
7. Schlüter, S. & Hoque, M. M. An SBAS integrity model to overbound residuals of higher-order ionospheric effects in the Ionosphere-free linear combination. *Remote Sens.* **12**(15), 2467 (2020).
8. Banville, S. GLONASS ionosphere-free ambiguity resolution for precise point positioning. *J. Geod.* **90**(5), 487–496 (2016).
9. Zhang, W. *et al.* Initial assessment of BDS-3 precise point positioning service on GEO B2b signal. *Adv. Space Res.: Off. J. Comm. Space Res.* **69**(1), 690–700 (2022).
10. Nie, Z. *et al.* Initial assessment of BDS PPP-B2b service: Precision of orbit and clock corrections, and PPP performance. *Remote Sens.* **13**(11), 2050 (2021).
11. Tang, C. *et al.* Orbit determination, clock estimation and performance evaluation of BDS-3 PPP-B2b service. *J. Geod.* **96**(9), 60 (2022).
12. Xu, Y., Yang, Y. & Li, J. Performance evaluation of BDS-3 PPP-B2b precise point positioning service. *GPS Solut.* **25**(4), 142 (2021).
13. Ren, Z. *et al.* Performance assessment of real-time precise point positioning using BDS PPP-B2b service signal. *Adv. Space Res.* **68**(8), 3242–3254 (2021).
14. Guo, J. *et al.* Assessment of multi-frequency PPP ambiguity resolution using Galileo and BeiDou-3 signals. *Remote Sens.* **13**(23), 4746 (2021).
15. Duong, V. *et al.* Assessing the performance of multi-frequency GPS, Galileo and BeiDou PPP ambiguity resolution. *J. Spat. Sci.* **65**(1), 61–78 (2020).
16. Laurichesse, D. & Banville, S. Instantaneous centimeter-level multi-frequency precise point positioning. *GPS World Innov. Column* **4**, 42–47 (2018).
17. Li, J. *et al.* An analytical study on the carrier-phase linear combinations for triple-frequency GNSS. *J. Geod.* **91**(2), 151–166 (2017).
18. Basile, F. *et al.* GPS and galileo triple-carrier ionosphere-free combinations for improved convergence in precise point positioning. *J. Navig.* **74**(1), 5–23 (2020).
19. Li, P. *et al.* Three-frequency BDS precise point positioning ambiguity resolution based on raw observables. *J. Geod.* **92**, 1357–1369 (2018).
20. Bu, J. *et al.* Performance assessment of positioning based on multi-frequency multi-GNSS observations: Signal quality, PPP and baseline solution. *IEEE Access* **9**, 5845–5861 (2020).
21. Xu, W. *et al.* Comparison and evaluation of carrier phase PPP and single difference time transfer with multi-GNSS ambiguity resolution. *GPS Solut.* **26**(2), 1–18 (2022).
22. Jianghui, G., Hua, C., General, G., Guangcai, L. & Na, W. Three multi-frequency and multi-system GNSS single-point high-precision positioning methods and performance analysis for complex urban environments. *J. Surv. Mapp.* **49**(01), 1–13 (2020).
23. Li, X. *et al.* Multi-GNSS phase delay estimation and PPP ambiguity resolution: GPS, BDS, GLONASS, Galileo. *J. Geod.* **92**(6), 579–608 (2018).
24. Duong, V. *et al.* An optimal linear combination model to accelerate PPP convergence using multi-frequency multi-GNSS measurements. *GPS Solut.* **23**(2), 1–15 (2019).
25. Khodabandeh, A. & Teunissen, P. J. G. An analytical study of PPP-RTK corrections: Precision, correlation and user-impact. *J. Geod.* **89**(11), 1109–1132 (2015).
26. Xiaohong, Z., Jiahuan, H. & Xiaodong, R. Comparison of PPP/PPP-RTK new progress and Beidou/GNSS PPP positioning performance. *J. Surv. Mapp.* **49**(09), 1084–1100 (2020).
27. Li, X. *et al.* Improving PPP-RTK in urban environment by tightly coupled integration of GNSS and INS[J]. *J. Geod.* **95**(12), 1–18 (2021).
28. Fan, C. *et al.* Ground-based PPP-RTK for pseudolite systems. *J. Geod.* **95**(12), 1–10 (2021).
29. Ge, H. *et al.* Initial assessment of precise point positioning with LEO enhanced global navigation satellite systems (LeGNSS). *Remote Sens.* **10**(7), 984 (2018).
30. Li, X. *et al.* LEO constellation-augmented multi-GNSS for rapid PPP convergence. *J. Geod.* **93**(5), 749–764 (2019).
31. Saastamoinen, J. Atmospheric correction for the troposphere and stratosphere in radio ranging satellites. *Use Artif. Satell. Geod.* **15**, 247–251 (1972).
32. Zengkai, S., Xurong, D., Yanfeng, H., *et al.* Development of Doppler-assisted improvement of pseudorange/carrier phase accuracy. In: proceedings of the 12th annual China satellite navigation conference - S07 satellite navigation enhancement technology, 2021.
33. Feiyang, W. & Li, X. Estimation and new characterization of phase fractional deviation of BeiDou-3 based on different PPP models[J]. *Global Positioning System.* **48**(01), 14–23 (2023)
34. Zhou, R. *et al.* Consistency analysis of the GNSS antenna phase center correction models. *Remote Sens.* **14**(3), 540 (2022).
35. Wu, J. T. *et al.* Effects of antenna orientation on GPS carrier phase. *Astrodynamics* **1992**, 1647–1660 (1991).
36. Zhao, H. *et al.* Determination of ocean tide loading displacement by GPS PPP with priori information constraint of NAO99b global ocean tide model. *Mar. Geod.* **41**(2), 159–176 (2018).
37. Hećimović, Ž. Relativistic effects on satellite navigation. *Tech. Gazette* **20**(1), 195–203 (2013).
38. Hu, W. & Farrell, J. A. Technical Note: Derivation of Earth-Rotation Correction (Sagnac) and Analysis of the Effect of Receiver Clock Bias. (2019).

39. Yaqiong, H. Research on key issues of precision single-point localization with BDS/GPS dual system [D]. University of Chinese Academy of Sciences (Institute of Precision Measurement Science and Technology Innovation, Chinese Academy of Sciences). <https://doi.org/10.27602/d.cnki.gkwsws.2021.000073> (2021).
40. Zhang, K. & Guo, G. Analysis of BDS-3 satellite performance enhancement for BDS global positioning. *Global Position. Syst.* **44**(06), 35–45 (2019).
41. Zhu, Y. *et al.* Comprehensive performance review of BDS-3 after one-year official operation. *Adv. Space Res.* **71**(1), 883–899 (2022).
42. Ye, F., Yuan, Y. & Yang, Z. Validation and evaluation on B1IB3I-based and B1CB2a-based BDS-3 precise orbits from iGMAS. *Adv. Space Res.* **70**(8), 2167–2177 (2022).
43. Zhang, Q., Zhu, Y. & Chen, Z. An in-depth assessment of the new BDS-3 B1C and B2a signals. *Remote Sens.* **13**(4), 788 (2021).
44. Wang, M. *et al.* Analysis of BDS/GPS signals' characteristics and navigation accuracy for a geostationary satellite. *Remote Sens.* **13**(10), 1967 (2021).
45. Yangfei, H., Junping, C., Yize, Z. (2022). PPP floating-point solution and fixed solution positioning accuracy analysis of BDS-3 new frequency (B1C+B2a) fused with GPS. In: proceedings of the 13th annual China satellite navigation conference. 1–6.
46. Zhang, R. *et al.* Ambiguity resolution for long baseline in a network with BDS-3 quad-frequency ionosphere-weighted model. *Remote Sens.* **14**(7), 1654 (2022).
47. Jie, L. *et al.* Clock difference estimation of two ionosphere-free combined orbits from BeiDou tri-frequency data and its application. *J. Surv. Mapp.* **49**(11), 1377–1387 (2020).

Acknowledgements

We thank Peng Li, Qin Liang, Yangzhuo Chen, Nianyu Yi, Xue Zhang and Juan Zhang for helpful discussions. This work is supported by the National Key Research and Development Program of China (Grants No. 2020YFA0713501).

Author contributions

C.L.C. and K.H.L. conceived the project. C.L.C. and K.H.L. established the carrier phase reconstruction theory and model and designed its algorithm; W.H.G. conducted Doppler reconstruction analysis; Z.X.L. conducted carrier phase reconstruction analysis; L.F.C. and M.J.W. conducted experimental verification; Y.H.C. helped revise the paper and made substantive suggestions; everything was under the supervision of W.H.G.; C.L.C. and K.H.L. wrote the manuscript with help from all authors.

Competing interests

The authors declare no competing interests.

Additional information

Correspondence and requests for materials should be addressed to C.C. or W.G.

Reprints and permissions information is available at www.nature.com/reprints.

Publisher's note Springer Nature remains neutral with regard to jurisdictional claims in published maps and institutional affiliations.



Open Access This article is licensed under a Creative Commons Attribution 4.0 International License, which permits use, sharing, adaptation, distribution and reproduction in any medium or format, as long as you give appropriate credit to the original author(s) and the source, provide a link to the Creative Commons licence, and indicate if changes were made. The images or other third party material in this article are included in the article's Creative Commons licence, unless indicated otherwise in a credit line to the material. If material is not included in the article's Creative Commons licence and your intended use is not permitted by statutory regulation or exceeds the permitted use, you will need to obtain permission directly from the copyright holder. To view a copy of this licence, visit <http://creativecommons.org/licenses/by/4.0/>.

© The Author(s) 2024, corrected publication 2024